THE JOURNAL OF PHYSICAL CHEMISTRY C
A JOURNAL OF THE AMERICAN CHEMICAL SOCIETY

pubs.acs.org/JPCC

Article

Indium-Doped Crystals of $SnSe_2$

Danrui Ni, Xianghan Xu, Zheyi Zhu, Yasemin Ozbek, Vesna Mikšić Trontl, Chen Yang, Xiao Yang, Alex Louat, Cephise Cacho, N. P. Ong, Pengpeng Zhang, Tonica Valla, and Robert J. Cava*

Cite This: J. Phys. Chem. C 2024, 128, 11054−11062

Read Online

ACCESS | Metrics & More | Article Recommendations | Supporting Information

ABSTRACT: Bulk crystals of undoped and In-doped (on the order of 1%) $SnSe_2$ were synthesized using a solid-state temperature-gradient method and characterized by diffuse reflection, Raman scattering, ARPES and STM studies. An n-to-p crossover was observed as a function of the indium concentration in Hall measurements at 300 K, but the Seebeck coefficient is n-type at that temperature for all studied indium concentrations. The measured resistivity at 300 K reaches a maximum at the minimum carrier concentration. Our results suggest a multiband semiconducting nature for doped $SnSe_2$, which provides insight into the exploration of enhanced thermoelectric performance and exotic electric behavior.

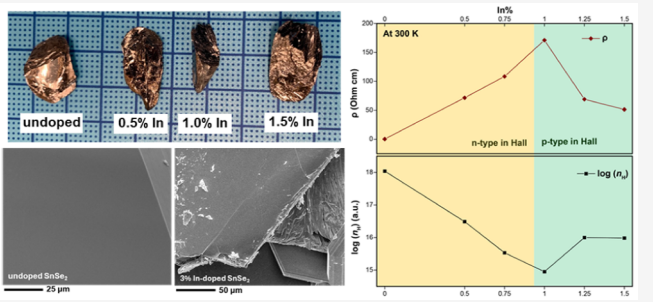

INTRODUCTION

Thermoelectric technology, with its capability to convert waste heat directly into electricity, has received increased attention due to the need for ecofriendly energy and stable, long-lasting power sources.[1−4] In searching for thermoelectric materials with higher performance, attempts have been made to increase the Seebeck coefficient (S) as well as decrease the electrical resistivity (ρ) and thermal conductivity (κ) of semiconductors, including band engineering, nanostructuring, and the fabrication of composite systems.[3−6]

Among the material candidates for thermoelectric applications, 2D van der Waals semiconducting materials, including layered metal dichalcogenides, such as MoS_2, SnS_2, and $SnSe_2$,[4,7−9] have attracted research interest due to their excellent electronic and transport properties.[2,3,10] As one of the promising candidates, $SnSe_2$, with its layered triangular lattice, suitable bandgap, and semiconducting band structure, has often been studied in this context.[2,6,8,11] Studies include intercalation,[12] doping,[13−15] layer engineering,[3,10,16] and microstructure modification,[17] revealing its potential for applications. As a commonly adopted material modification technique, we hypothesize that doping may trigger distinct behaviors, and introduce interesting properties to layered $SnSe_2$. As $SnSe_2$ itself is reported to be n-type (as confirmed here), indium seems to be a promising dopant to employ for Sn^{4+} substitution to achieve compensation due to its similar atomic size and its +3 valence. However, the bulk crystal growth and electronic properties of In-doped $SnSe_2$ have not been reported. SnS_2, the isostructural sulfide compound, has been studied in an In-doped monolayer.[18] The material was obtained through mechanical cleavage from a chemically vapor-transported bulk crystal, and a transition from n- to p-type behavior was reported. Meanwhile, In-doped $SnSe_2$ has been synthesized as nanosheets using a hydrothermal method and studied as a sulfur dioxide gas sensor.[15]

Undoped $SnSe_2$ is always an n-type semiconductor due to the presence of a small number of vacant Se sites. In Kröger-Vink notation, the defect chemistry of undoped $SnSe_2$ is

$$Se_{Se} \rightarrow V_{Se}^{\bullet\bullet} + 2e' + Se(g)\uparrow \quad (1)$$

yielding n-type behavior.

For indium doping, the subject of this work, the following two processes appear to compete:

In substituting on the Sn site in

$$SnSe_2 \rightarrow In_{Sn}' + h^{\bullet} \quad (2)$$

In intercalating between the layers in

$$SnSe_2 \rightarrow In_i^{\bullet\bullet\bullet} + 3e' \quad (3)$$

Here we report the synthesis and electronic properties of a series of $SnSe_2$ crystals doped with Indium, in the composition range between 0.5 and 1.5%, obtained by cooling from a melt. The low indium doping levels employed were designed to compensate for the selenium vacancies normally present, which lead to n-type behavior (eq 1). Various physical and electrical properties were characterized by using comprehen-

Received: May 3, 2024
Revised: May 31, 2024
Accepted: June 10, 2024
Published: June 18, 2024

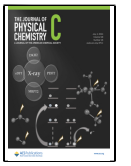

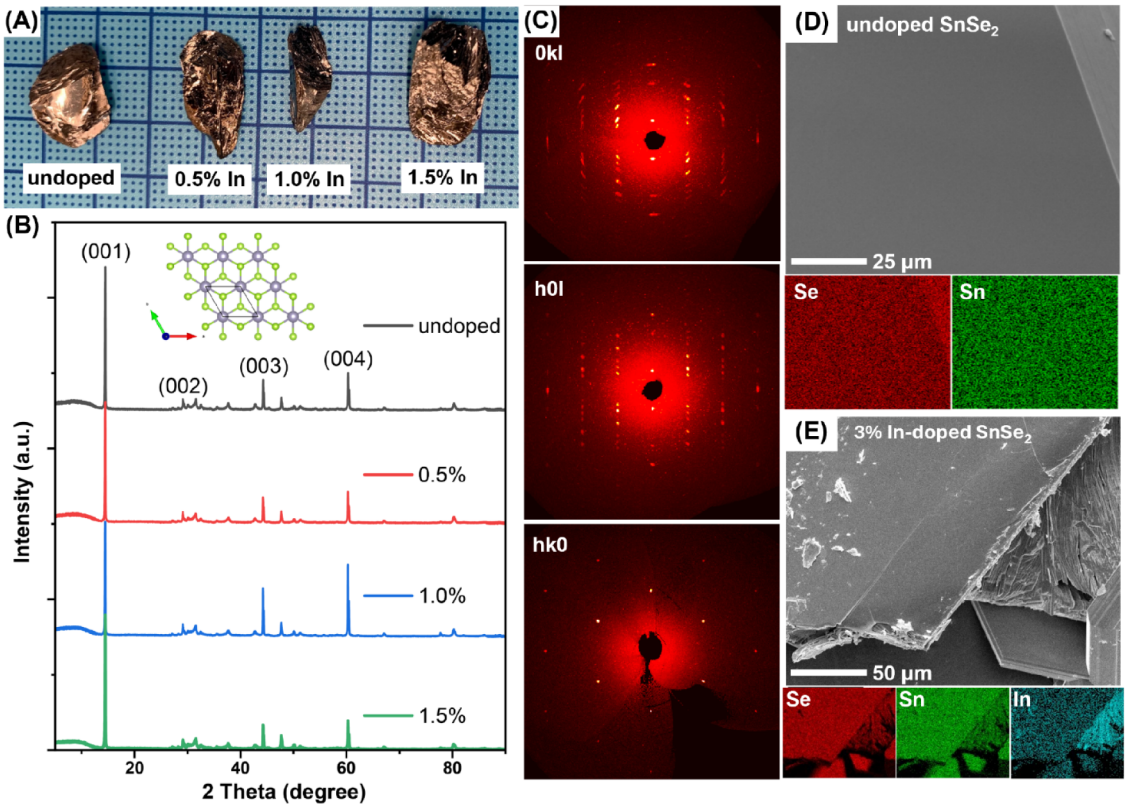

Figure 1. Structural characterization: (A) photos of $SnSe_2$ crystals. (B) PXRD patterns of undoped, and 0.5%, 1.0%, 1.5% In-doped sample powders, ground from the as-grown crystals; Multiple polytypes may coexist in $SnSe_2$, and thus the (00l) peaks are labeled with the Miller indices based on a single-layer unit cell. (C) The 0kl (top), h0l (middle), and hk0 (bottom) reciprocal lattice planes of one undoped $SnSe_2$ single crystal. SEM images are shown with EDX element maps for undoped (D) and 3% In-doped $SnSe_2$ (E).

sive experimental probes, revealing unexpected behavior. An n-to-p crossover is detected in the Hall-effect-determined carrier concentration at 300 K, with the Seebeck coefficient being n-type for all $SnSe_2$ samples at the same temperature. This kind of behavior is relatively rare in conventional semiconductors like $SnSe_2$, although it has been reported previously for magnetic, disordered, and amorphous systems. Our evidence is that processes (2) and (3) occur at the same time in In-doped $SnSe_2$, with the first process being dominant (yielding holes) in the beginning stages of doping and the second process being highly influential (i.e., yielding electrons) by a ∼ 1.25% Indium doping level.

EXPERIMENTAL METHODS

Material Synthesis. The undoped and doped $SnSe_2$ crystals were prepared by a temperature gradient method.[2] Elemental starting materials (Sn granules, Alfa Aesar 99.5+%; Se shot, amorphous, Alfa Aesar 99.999+%; and indium shot, Alfa Aesar Puratronic 99.9995%) were weighed stoichiometrically with formulas $Sn_{1-x}In_xSe_2$, with different indium doping amounts (x = 0, 0.005, 0.0075, 0.010, 0.0125, 0.015), and sealed under vacuum in quartz ampules. Batch sizes were on the order of 5 g. They were heated to 750 °C, soaked for 12 h, and then cooled at 5 °C/h to 550 °C. Samples were annealed at 550 °C for 1 day and then cooled to room temperature at 3 °C/min. The crystals obtained were silvery in color with a layered morphology.

Structural Characterization and Spectroscopy. Single-crystal X-ray diffraction (SCXRD) was performed at 300 K on a Bruker D8 Quest Eco diffractometer with a Photon III CPAD detector and Mo Kα radiation (λ= 0.71073 Å) primarily to determine the unit cell symmetry and dimensions. Laboratory powder X-ray diffraction (PXRD) patterns were collected at 300 K on a Bruker D8 Advance ECO diffractometer with Cu Kα radiation (λ = 1.5406 Å). Structure refinement was performed using the SHELXTL Software Package.[19,20] Scanning electron microscopy (SEM) images of as-grown crystals were collected with a Quanta 200 FEG Environmental-SEM.

UV−vis diffuse reflectance data were collected on an Agilent Cary 5000 spectrometer with an Agilent Internal DRA-2500 diffuse reflectance accessory. The reflectance data were converted to absorption by using the Kubelka−Munk function, and the band gap values were evaluated by using Tauc plots. Raman spectra were collected on a Thermofisher DXR3xi spectrometer at room temperature with baseline correction.[21] The Raman peaks were analyzed by using Gaussian fits with Matlab R2024a.

STM. Samples were mounted on blank sample plates using silver epoxy cured in a furnace at 150 °C under nitrogen gas for an hour. They were then transferred into an Omicron low-temperature scanning tunneling microscope chamber under ultrahigh vacuum (UHV) conditions and cleaved *in situ,* after which STM and scanning tunneling spectroscopy (STS) were utilized for characterization after the samples were cooled to liquid nitrogen temperatures (∼77.5K) overnight at a base pressure of 1.8×10^{-11} mbar. To survey the morphology of the doped samples, the tip was first rastered over the cleaved sample surface at 4 V and 10 pA for a sufficient amount of time to sweep away the indium atoms that had been intercalated

https://doi.org/10.1021/acs.jpcc.4c02926
J. Phys. Chem. C 2024, 128, 11054−11062

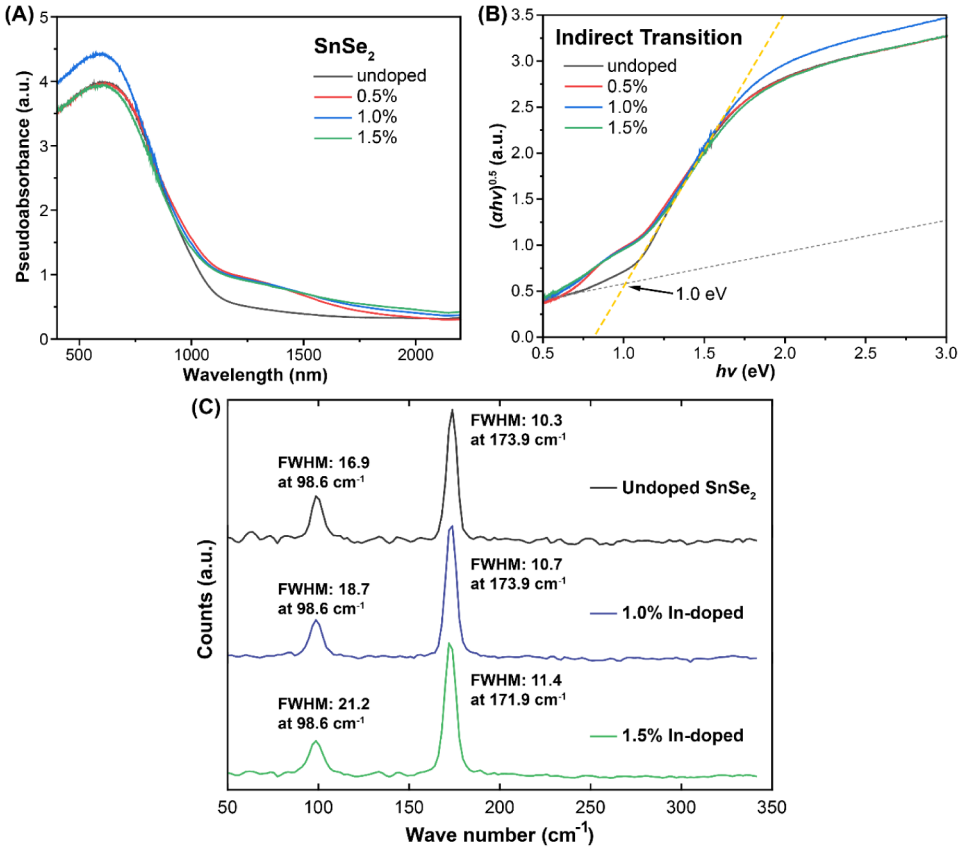

Figure 2. Optical characterization. (A) Pseudoabsorbance spectra of undoped and In-doped $SnSe_2$ powder samples, measured by diffuse reflectance spectroscopy, with (B) the Tauc plots of indirect transitions. (C) Raman spectra of undoped, 1.0%, and 1.5% In-doped $SnSe_2$. The results of the fits are shown.

between the $SnSe_2$ atomic layers. The tip was then brought closer to the sample surface for atomically resolved imaging. STS spectra were obtained using a lock-in amplifier with the modulation signal set at 26 meV in amplitude and 1.1 kHz in frequency. The STM tip was calibrated by measuring reference spectra on a silver substrate to avoid tip artifacts.

ARPES. The angle-resolved photoemission spectroscopy (ARPES) experiments were carried out at the I05 beamline at the Diamond synchrotron with an MBS electron spectrometer and photons in the range of 60 to 105 eV. The total instrumental energy resolution was ∼8 meV. Angular resolution was better than ∼0.15 deg and 0.2 deg along and perpendicular to the slit of the analyzer, respectively. The samples were cleaved in the ARPES chamber (base pressure of 1×10^{-10} mb) and studied at 10 K. On some samples, small doses of K were evaporated *in situ* to increase the filling of the conduction band.

Transport and Thermopower Property Characterization. Resistivity and Hall effect measurements were carried out using a Quantum Design PPMS-9 (DynaCool) on crystals cut into rectangular pieces using a four-probe method with electrodes made from silver epoxy. Temperature-dependent resistivity was measured under zero magnetic field, while magnetic-field-dependent Hall resistivity data were collected at 300 K. The presented Hall data have been antisymmetrized. All transport measurements were performed on crystal plates normal to the *c* axis prepared by cleaving.

Thermopower measurements were conducted at room temperature in an ambient atmosphere. The crystals were cut into rectangular pieces (about 1 mm × 5 mm, with the thickness varying between 100 and 300 μm) for the measurements. The crystal pieces were suspended by two silicon substrates along the long direction, and a small amount of thermal joint compound was used to ensure thermal contact between the crystal and substrate. An 800 ohm heater was fixed on one substrate with GE varnish to create a thermal gradient across the sample. A Type E thermocouple was used to measure the thermal gradient, and two small pieces of cigarette paper were placed between the thermocouple joint and the crystal to avoid shorting. The electrical contacts for the thermopower voltage measurement were fixed with silver paint on the sample. Thermopower (Seebeck coefficient) was calculated as $S = -\frac{\Delta V / L_{\text{contact}}}{\Delta T / L_{\text{thermocouple}}}$ (the electric field and the thermal gradient were assumed to be approximately uniform along the suspended part of sample), where L_{contact} is the length between two thermopower contacts, and $L_{\text{thermocouple}}$ is the length between two thermocouple joints, and we used the centers of the silver paint contacts to give best estimation of these two lengths.

RESULTS AND DISCUSSION

Examples of the undoped and In-doped $SnSe_2$ crystals obtained are shown in Figure 1A. The PXRD patterns were collected on the powders ground from the crystals. Similar patterns are observed, confirming the triangular layered structure for all materials (Figure 1B), both undoped and doped; a strong preferred orientation of the (00l) peaks can be

https://doi.org/10.1021/acs.jpcc.4c02926
J. Phys. Chem. C 2024, 128, 11054−11062

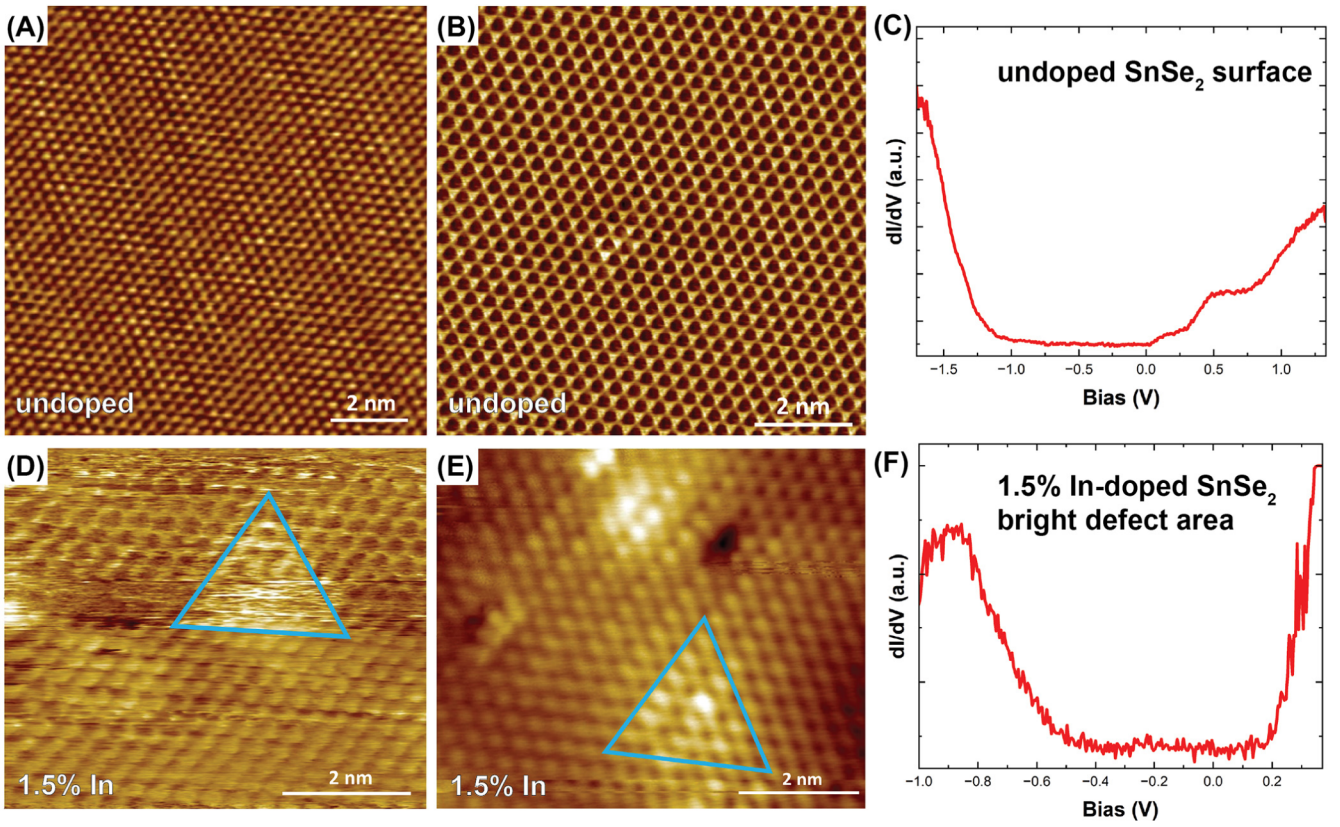

Figure 3. STM images of undoped $SnSe_2$ at (A) 1.2 V, 50 pA and (B) 1.7 V, 30 pA, with the STS spectrum of the sample surface in (C); and 1.5% In-doped $SnSe_2$ at (D) −1.8 V, 30 pA, where there are still mobile ions on the surface, causing the streaked appearance; and (E) −1.8 V, 50 pA, after the local area has been swept clean by the scanning tip. The blue triangles label the surface defect features in In-doped $SnSe_2$, and the STS result for that surface is shown in (F).

observed in all of the patterns (labeled with Miller indices based on a single-layer unit cell in the figure), with a very small position shift for some high angle peaks. $SnSe_2$ is commonly noted to have $P\bar{3}m1$ symmetry with a *c*-axis characteristic of a single-layer structure (with Sn at the 1*a* and Se at the 2*d* Wyckoff sites), but very small extra peaks can be observed in our PXRD patterns, matching the PDF 00−038−1055 $SnSe_2$ pattern in the PXRD database. These small extra peaks are due to polytypes originating from differences in the layer stacking, consistent with previous reports; more than ten polytypes have been reported for $SnSe_2$.[22,23] Single crystal refinements were attempted in order to determine the structural details of an 18R structure (which has been reported previously in ref. 8); however, the stacking faults and multiple polytypes present made it impossible to do so, as has been seen in other $SnSe_2$ studies, with the structures of the different polytypes usually determined by electron diffraction.[8,22,23] The reciprocal-lattice planes of a single crystal of $SnSe_2$ are shown in Figure 1C, with some streaking seen in the h0l plane, confirming the presence of the polytypism. For undoped $SnSe_2$, our Le Bail fitting of the PXRD pattern (Figure S1) resulted in a = 3.8128(1) Å and c = 55.223(1) Å. The effect of stacking faults can be clearly observed in the PXRD fitting through the asymmetric shape of the small peaks. The structural analysis confirms our successful synthesis of $SnSe_2$ with triangular layers and the existence of polytypism in our materials with the 18R polytype dominant.

SEM images show the smooth surfaces of the $SnSe_2$ layers (Figure 1D). EDX mapping reveals uniformly distributed Sn and Se in about a 1:2 ratio for undoped $SnSe_2$ (Figure S2). However, at indium doping ratios higher than 1.5%, the $SnSe_2$ lattice reaches its limit to solubilize the indium dopant, and the excess indium present crystallizes in a separate phase. As shown in Figures 1D and S2, for example, in a 3% In-doped $SnSe_2$ sample, a layer with obviously different morphologies and much higher indium contents can be observed. Therefore, in this report, our characterization focuses on $SnSe_2$ samples with indium doping amounts no higher than 1.5%.

Diffuse reflectance spectra were collected on ground powders of undoped and the 0.5%, 1.0%, and 1.5% In-doped $SnSe_2$ samples (Figure 2A). Previous work has established (confirmed by our ARPES data) that $SnSe_2$ has an indirect transition, and thus the band gaps of the current materials can be estimated using Tauc plots (Figure 2B) with the equation:[24,25]

$$(\alpha h\nu)^{0.5} = K(h\nu - E_g) \tag{4}$$

where K is a constant and α is the absorption coefficient (cm^{-1}). The absorption between 750 and 1200 nm is attributed to the band gap absorption and is relatively consistent for the measured samples. Therefore, consistent with expectations at the relatively low indium doping levels studied here, the band gap is relatively independent of doping and is estimated to be about 1.0 eV. The Tauc plot method, although commonly adopted, can sometimes underestimate the band gap energy as it ignores subband gap contributions that can be misinterpreted as an indirect transition.[26] Our obtained band gap value is consistent with the literature for the indirect transition of bulk undoped $SnSe_2$.[27,28] A weak

https://doi.org/10.1021/acs.jpcc.4c02926
J. Phys. Chem. C 2024, 128, 11054−11062

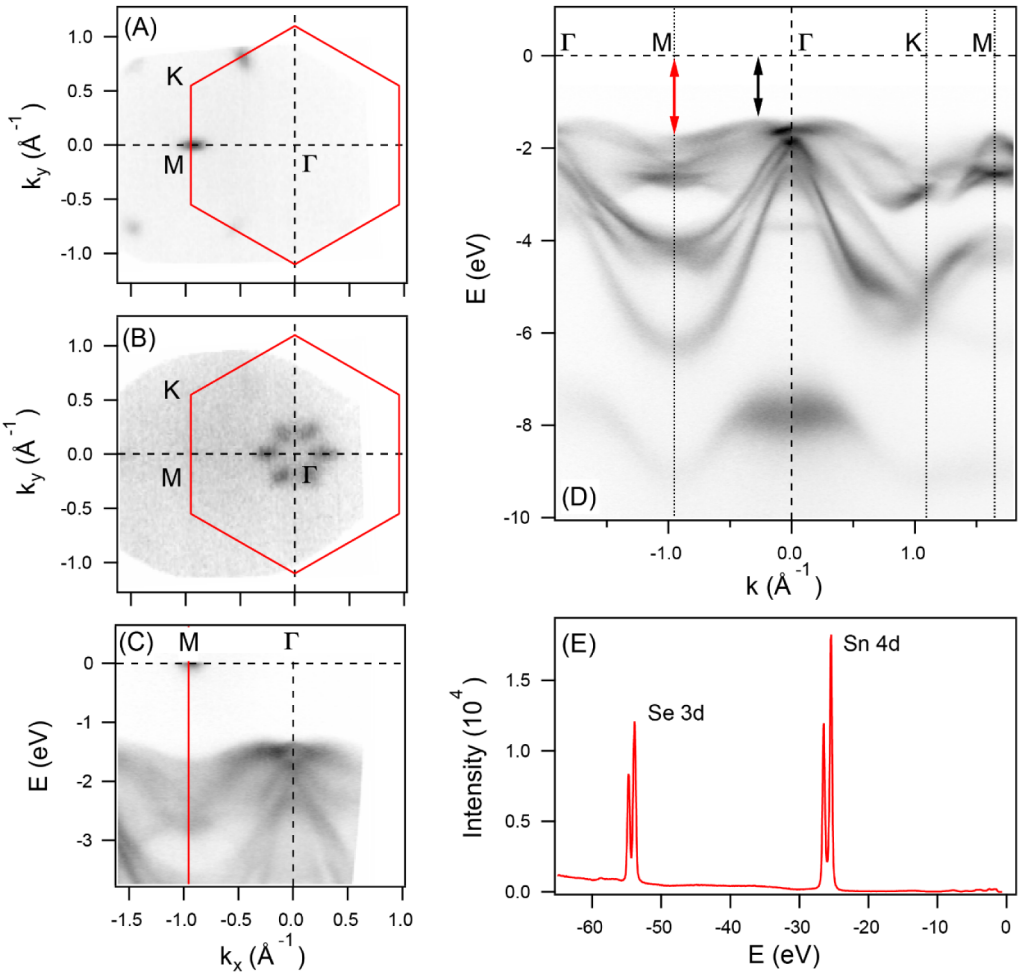

Figure 4. The momentum-resolved electronic structure of $SnSe_2$. (A) ARPES intensity at the Fermi level, $E = 0$ (Fermi surface), and (B) at $E = -1.26$ eV, the energy corresponding to the VBM; (C) ARPES intensity along the $k_y = 0$ line, corresponding to the GM line in the BZ, indicating dispersion of the valence band and position of the conduction band minimum. (D) Wide energy range experimental band structure of the pristine $SnSe_2$ surface along the GM and GK high symmetry lines. The black and red arrows indicate the magnitudes of indirect (1.26 eV) and direct (1.6 eV) transitions, respectively. (E) Photoemission spectrum of the shallow core levels in the pristine $SnSe_2$. In (A-C), the small dose (<0.1 monolayer) of potassium was evaporated on the surface to increase the occupation of the conduction band. The photon energy used in (A−C) and (D,E) was 70 and 100 eV, respectively.

absorption tail can be observed for the doped samples at around 1300 nm, corresponding to an additional transition at around 0.6 eV, which can be attributed to transitions from a defect band introduced by the doping within the band gap,[29] consistent with our STM data.

Raman spectra were collected on undoped, 1.0% In, and 1.5% In-doped $SnSe_2$ crystals (Figure 2C), the latter of which are very close to the minimum electron concentration. Two Raman-active phonon modes can be observed: an in-plane stretching mode (E_g) at around 100 cm^{-1}, and an out-of-plane stretching mode (A_{1g}) at around 174 cm^{-1}.[15,30] For the potential impurity In_2Se_3,[31] there should be Raman-active In−Se stretching modes in the range of 100−250 cm^{-1}, which were not seen in our In-doped $SnSe_2$. Comparing the spectrum of undoped and 1% doped batches, the peak positions do not obviously move, but the peaks turn a bit wider (especially for the E_g mode), suggesting that the small amount of indium dopant present slightly might distort the in-plane lattice.

When the Raman spectrum of 1.5% In-doped $SnSe_2$ is compared (Figure 2C bottom), a peak shift of the out-of-plane stretching mode can be observed together with the peak widening, consistent with our conclusion that the indium is now exceeding the hosting ability of the Sn sublattice and clearly intercalating between the $SnSe_2$ layers, which more obviously affects the out-of-plane stretching.

The high-resolution STM images in Figure 3A,B confirm the triangular lattice of the pristine $SnSe_2$ layers. Undoped $SnSe_2$ has a low defect density but has a relatively high n-type carrier concentration due to the presence of the small number of vacant Se sites (eq 1). This leads to a conduction band minimum (CBM) close to the Fermi level, as seen in the STS-measured results (Figure 3C). The band gap is close to 1 eV, which is consistent with the diffuse reflectance measurement. Figures 3D,E show the STM images of 1.5% In-doped $SnSe_2$, which are distinct from those of undoped $SnSe_2$. The doped sample has defect features on its surface (shown as dark dots and bright defect areas, as labeled in the images), which may correspond to in-plane doping, and a distinct doping feature is detected with a band gap at ∼0.6 eV from STS in Figure 3F (consistent with the estimated value of the weak absorption transition from defect bands, seen in the diffuse reflectance spectra).

https://doi.org/10.1021/acs.jpcc.4c02926
J. Phys. Chem. C 2024, 128, 11054−11062

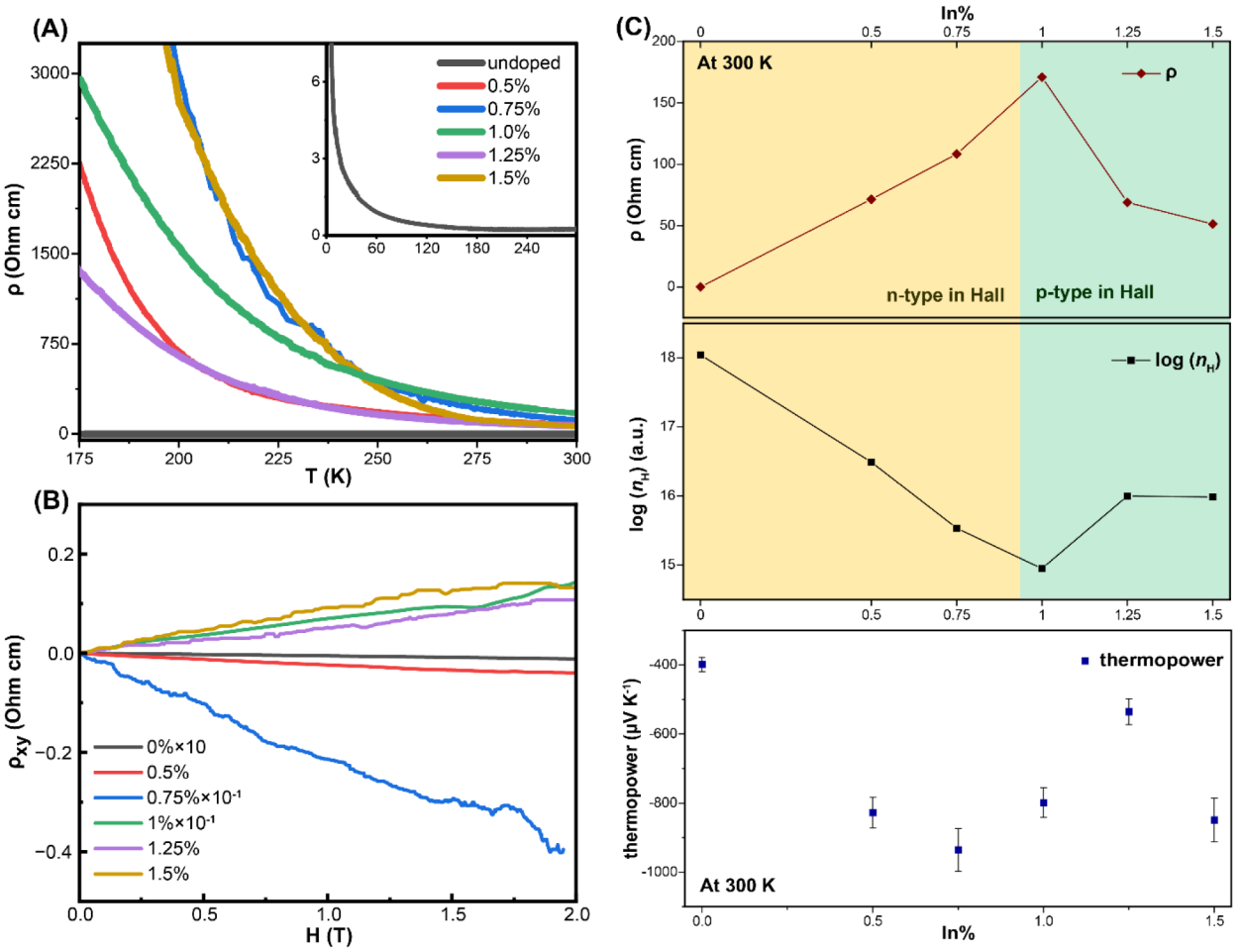

Figure 5. Electrical characterization. (A) Temperature-dependent resistivity (ρ) and (B) magnetic-field-dependent Hall resistivity (ρ_{xy}) of $SnSe_2$ crystals. The resistivity (top), net Hall carrier concentration (middle), and Seebeck coefficient (bottom) at 300 K are plotted versus indium doping ratio in (C).

Additionally, different from the flat and clean cleaved surface of undoped $SnSe_2$, there are mobile ions on the surface of 1.5% In-doped $SnSe_2$, making it challenging to reach atomic resolution. Figure 3D illustrates such a surface, where, in this case, the mobile ions have not been completely swept away by the scanning tip. This is likely related to the fact that at these doping levels, the indium intercalates between the $SnSe_2$ layers in significant amounts. For real-space exploration of the indium intercalation between the $SnSe_2$ layers, high-resolution scanning transmission electron microscopy studies (such as HAADF-STEM)[12,32] may be of future research interest.

Figure 4 shows the momentum-resolved electronic structure of $SnSe_2$, obtained directly from our ARPES study. The cleaved pristine sample (in panels D and E) shows almost no intensity at the Fermi level. The top of the valence band (VB) is near Γ, but not exactly—there are 6 valence band maxima (VBM) along the Γ-M lines, slightly displaced from Γ. At energies slightly below the VBM, the VB forms six ellipsoidal contours, as illustrated in the panel (B). In the case of low hole doping, these contours would form the first hole pockets. In the pristine samples, the Fermi level is pinned to the bottom of the conduction band (CB). However, only traces of intensity at the Fermi level, just above the noise level, could be found at M points in the Brillouin Zone (BZ). To make these electron pockets more visible and to determine their position, shape, size, and dispersion, we have deposited small amounts of potassium on the cleaved surfaces of undoped $SnSe_2$. This resulted in electrons entering the CB in significant amounts. At the M point, at a coverage of only 0.06 monolayers of potassium, ellipsoidal electron pockets are already well formed; their intensity is comparable to the intensity at the VBM. This is shown in Figure 4A–C. The pockets grew proportionally with increasing potassium coverage, enabling not only an estimation of their volume but also, by extrapolation zero coverage, yielding an estimate for the electron concertation of the undoped sample. By approximation of the pockets with ellipsoids, the carrier concentrations are approximately $n = 3 \times 10^{18}$ cm^{-3} and 9×10^{17} cm^{-3}, for the potassium-dosed (Figure 4A–C) and undoped samples, respectively. The calculation of carrier concentration via ARPES involves measurement of the Fermi surface volume and is therefore sensitive to the dimensionality of the system. For a three-dimensional system, the measurements should also include the determination of the Fermi wavevectors in the out-of-plane direction (k_z). However, in that direction, the accuracy of ARPES is very limited due to its limited probing depth. The band structure calculations for this material[8] and our photon energy dependent studies indicate that although the system is quasi 2D, the dispersion along k_z is not negligible. Therefore, our carrier concentration estimate has been done on the assumption that the electron Fermi pockets are ellipsoids with a long axis along Γ-M and that the other two axes are equal and two times shorter.

https://doi.org/10.1021/acs.jpcc.4c02926
J. Phys. Chem. C 2024, 128, 11054−11062

Table 1. Transport Activation Energy (Ea), as Well as Hall Coefficient (R_H), Net Hall Carrier Concentration (n_H), Hall Mobility (μ_H), and Seebeck Coefficient (S) at 300 K, of Undoped and In-Doped $SnSe_2$ Samples

In%	Ea (eV)	R_H ($cm^3\ C^{1-}$)	n_H (cm^{-3})	μ_H ($cm^2\ V^{-1}\ s^{-1}$)	S ($\mu V\ K^{-1}$)
0	0.01	−5.67	-1.1×10^{18}	43.8	−399
0.5%	0.12	−201	-3.1×10^{16}	2.8	−828
0.75%	0.17	-1.84×10^3	-3.4×10^{15}	17.0	−935
1.0%	0.11	7.01×10^3	8.9×10^{14}	41.0	−799
1.25%	0.27	624	1.0×10^{16}	9.1	−535
1.5%	0.27	650	9.6×10^{15}	12.7	−849

Nonetheless, the carrier concentration and type (electrons) obtained in this way agree amazingly well with the Hall measurements on the undoped sample.

The VB was rigidly shifted down during the K-deposition by the same amount as the CB, with no other visible changes, keeping the gap between them constant. It is clear from Figure 4D that the gap in $SnSe_2$ is indirect, with a magnitude of about 1.2 eV. The minimal direct gap occurs at the M point, with a magnitude of about 1.6 eV.

The temperature-dependent resistivity ρ of $SnSe_2$ samples between 300 and 175 K is plotted in Figure 5A. All of the samples show semiconducting behavior. The approximate resistivity activation energy Ea can be calculated by the linear fitting of $\ln(\rho)$ versus $1/T$ plots and is listed in Table 1. The very small value of Ea, especially for undoped $SnSe_2$, is a reflection of its n-type nature, consistent with the ARPES measured results, for example, which show a significant number of electrons in the conduction band even at 10 K.

Hall measurements were conducted at 300 K at different indium doping ratios, and the Hall resistivity ρ_{xy} is plotted versus magnetic field in Figure 5B. The sign of the slope indicates the dominant carrier type (positive slope for the p-type and negative slope for the n-type), while a smaller slope corresponds to a higher net Hall carrier concentration. It is observed that our undoped $SnSe_2$ is n-type with a relatively high carrier concentration, while with indium doping, the resistivity obviously increases and the Hall effect becomes less n-type. A switch from n- to p-type behavior in the Hall effect can be observed between 0.75% and 1.0%. In-doped $SnSe_2$ and both 0.75% and 1.0% samples are observed to have relatively high resistivity in the ρ vs T plots.

The Hall coefficient R_H and net Hall carrier concentrations n_H can be calculated based on the measurements and are also presented in Table 1. The carrier concentration of undoped $SnSe_2$ is close to the value estimated by ARPES. Thus, as viewed in Figure 5C, at 300 K, the In-doped $SnSe_2$ series can be separated into two parts with the n-to-p crossover point based on Hall measurements. With initially increasing indium content (the left branch), the net carrier concentration measured by the Hall effect obviously decreases, reaches a minimum value at the n-to-p crossover, and then rebounds in value (the right branch). Meanwhile, the resistivity at 300 K varies with the opposite trend, which, with more indium added, increases first, reaches a maximum at about 1% doping, and then decreases. The 1.25% and 1.5% samples have similar net carrier concentrations and close resistivity values at 300 K, associated with the "overdoping" mentioned previously. Thus, the trends observed in the resistivity and Hall measurements are consistent with an increase in p-type doping with increasing In-for-Sn substitution, as expected. The Hall mobility μ_H at 300 K can also be estimated using the Drude model ($\mu_H = \frac{1}{\rho n_H e}$, where e is the charge of electron) based on the measured results. The calculated value for our undoped $SnSe_2$, about 44 $cm^2V^{-1}S^{1-}$, is of the same magnitude as that reported by others.[2] Unfortunately, the estimates of mobility with the Drude model assume a single dominant carrier type, and errors are likely to be introduced when the mobilities are estimated for the doped samples.

Thermopower measurements, on the other hand, indicate that the material has a negative Seebeck coefficient (S) for both undoped and Indium-doped $SnSe_2$ at 300 K. The estimated values of S are listed in Table 1 and Figure 5C. For the undoped sample, S is around $-400\ \mu V\ K^{-1}$, which is again consistent with the literature.[33] With indium doping, the absolute value of the negative Seebeck coefficient increases, with the highest value obtained at 0.75% In-doped $SnSe_2$, consistent with expectations for a lower carrier concentration semiconductor. As high thermopower is favored for thermoelectric applications, this doping-induced increase in the Seebeck coefficient may be of future research interest, although the dramatic increase in resistivity may limit the usefulness of this material.

While relatively rare, opposite signs in Hall and Seebeck measurements have been observed previously in other doped semiconducting systems,[34] and can be explained by a multiband system where two types of carriers coexist in the material, consistent with our picture for In-doped $SnSe_2$. As a defect band (or an "impurity band") was observed in our diffuse reflectance and STS measurements, we can apply a two-band model, with R_H and S represented by[35−37]

$$R_H = \frac{1}{n_H e} = \frac{n_h\mu_h^2 - n_e\mu_e^2}{e(n_h\mu_h + n_e\mu_e)^2} \quad (5)$$

$$S = -\frac{\Delta V}{\Delta T} = \frac{S_h n_h\mu_h - S_e n_e\mu_e}{n_h\mu_h + n_e\mu_e} \quad (6)$$

where n_i is the carrier concentration, μ_i is the mobility, and S_i is the Seebeck coefficient for each carrier. With two different types of carriers in the system at 300 K, the different values of n, S, and especially μ of the holes and electrons may result in an opposite sign for the Hall and Seebeck coefficients. An alternate explanation may be the temperature variation of the signs for Hall and/or Seebeck coefficient, such as for doped LaZnOP, transition-metal-doped InP, and Ni-doped $CoSb_3$.[5,37,38] As the two temperature-dependent changes are not required to occur at the same temperature, there can be a temperature range where Hall and Seebeck coefficients have opposite signs (thus, measurements at different temperatures may be of future interest). Another possible explanation is that for layered semiconducting materials, there may be a surface accumulation layer with different dominant carrier type than is seen in the bulk.[39]

https://doi.org/10.1021/acs.jpcc.4c02926
J. Phys. Chem. C 2024, 128, 11054−11062

CONCLUSIONS

Using a temperature gradient solid-state method, bulk crystals of undoped and In-doped $SnSe_2$ were prepared. With increasing indium doping, an n-to-p crossover was observed in Hall measurements at 300 K, with the Seebeck coefficient, however, showing n-type behavior for all doped $SnSe_2$ samples at the same temperature. Our data are consistent with the presence of a competition between In substitution and In intercalation for all compositions, and thus, mixed *n*- and p-type conductivity. The maximum In for Sn substitution possible for obtaining single-phase layered Indium-doped $SnSe_2$ appears to be between 1.25 and 1.5%. This study provides further insight into the doping of $SnSe_2$, and it may inspire its design, fabrication, and modification for new functional materials, which have potential capabilities for applications in next-generation electronic devices.

ASSOCIATED CONTENT

Supporting Information

The Supporting Information is available free of charge at https://pubs.acs.org/doi/10.1021/acs.jpcc.4c02926.

Le Bail fitting of undoped $SnSe_2$ PXRD pattern and detailed SEM/EDX analyses listing the contents of the material supplied as Supporting Information (PDF)

AUTHOR INFORMATION

Corresponding Author

Robert J. Cava − *Department of Chemistry, Princeton University, Princeton, New Jersey 08544, United States;* orcid.org/0000-0002-3294-6867; Email: rcava@princeton.edu

Authors

Danrui Ni − *Department of Chemistry, Princeton University, Princeton, New Jersey 08544, United States;* orcid.org/0000-0001-6916-1281

Xianghan Xu − *Department of Chemistry, Princeton University, Princeton, New Jersey 08544, United States;* orcid.org/0000-0001-6854-300X

Zheyi Zhu − *Department of Physics, Princeton University, Princeton, New Jersey 08544, United States*

Yasemin Ozbek − *Department of Physics and Astronomy, Michigan State University, East Lansing, Michigan 48824-2320, United States;* orcid.org/0000-0002-7711-7720

Vesna Mikšić Trontl − *Institut za fiziku, Zagreb HR-10000, Croatia;* orcid.org/0000-0002-9390-568X

Chen Yang − *Department of Chemistry, Princeton University, Princeton, New Jersey 08544, United States;* orcid.org/0000-0003-0162-0319

Xiao Yang − *Department of Physics, Princeton University, Princeton, New Jersey 08544, United States*

Alex Louat − *Diamond Light Source Ltd, Harwell Science and Innovation Campus, Didcot OX11 0DE, United Kingdom*

Cephise Cacho − *Diamond Light Source Ltd, Harwell Science and Innovation Campus, Didcot OX11 0DE, United Kingdom*

N. P. Ong − *Department of Physics, Princeton University, Princeton, New Jersey 08544, United States*

Pengpeng Zhang − *Department of Physics and Astronomy, Michigan State University, East Lansing, Michigan 48824-2320, United States;* orcid.org/0000-0002-9541-4884

Tonica Valla − *Donostia International Physics Center, Donostia-San Sebastian 20018, Spain*

Complete contact information is available at: https://pubs.acs.org/10.1021/acs.jpcc.4c02926

Notes

The authors declare no competing financial interest.

ACKNOWLEDGMENTS

This research was funded by the Gordon and Betty Moore Foundation, EPiQS initiative, Grant No. GBMF-9066. X. Xu acknowledges the US Department of Energy grant DE-FG02-98ER45706. T. V. acknowledges the support from the Red guipuzcoana de Ciencia, Tecnología e Innovacíon− Gipuzkoa NEXT 2023 from the Gipuzkoa Provincial Council. V. M. T. acknowledges the support of the Centre for Advanced Laser Techniques (CALT), grant KK.01.1.1.05.0001. The ARPES work was carried out with the support of Diamond Light Source, instrument i05 (proposal SI36637-1). The thermopower experiments were supported by the NSF MRSEC grant DMR-2011750. The STM/STS experiments were supported by the U.S. Department of Energy (DOE), Office of Basic Energy Sciences, Division of Materials Sciences and Engineering under Award Number DE-SC0019120. P. P. Zhang acknowledges the financial support from National Science Foundation (DMR-2112691). The authors acknowledge the use of Imaging and Analysis Center (IAC) operated by the Princeton Materials Institute at Princeton University, which is supported in part by a National Science Foundation (NSF) Materials Research Science and Engineering Center (MRSEC; DMR-2011750).

REFERENCES

(1) Wang, Y.; Yang, L.; Shi, X.-L.; Shi, X.; Chen, L.; Dargusch, M. S.; Zou, J.; Chen, Z.-G. Flexible Thermoelectric Materials and Generators: Challenges and Innovations. *Adv. Mater.* **2019**, *31* (29), 1807916.

(2) Pham, A.-T.; Vu, T. H.; Cheng, C.; Trinh, T. L.; Lee, J.-E.; Ryu, H.; Hwang, C.; Mo, S.-K.; Kim, J.; Zhao, L.; et al. High-Quality $SnSe_2$ Single Crystals: Electronic and Thermoelectric Properties. *ACS Appl. Energy Mater.* **2020**, *3* (11), 10787−10792.

(3) Li, G.; Ding, G.; Gao, G. Thermoelectric Properties of $SnSe_2$ Monolayer. *J. Phys.: Condens. Matter.* **2017**, *29* (1), 015001.

(4) Li, D.; Gong, Y.; Chen, Y.; Lin, J.; Khan, Q.; Zhang, Y.; Li, Y.; Zhang, H.; Xie, H. Recent Progress of Two-Dimensional Thermoelectric Materials. *Nano-Micro Lett.* **2020**, *12* (1), 36.

(5) Kitagawa, H.; Wakatsuki, M.; Nagaoka, H.; Noguchi, H.; Isoda, Y.; Hasezaki, K.; Noda, Y. Temperature Dependence of Thermoelectric Properties of Ni-Doped $CoSb_3$. *J. Phys. Chem. Solids* **2005**, *66* (10), 1635−1639.

(6) Kumar, M.; Rani, S.; Singh, Y.; Gour, K. S.; Singh, V. N. Tin-Selenide as a Futuristic Material: Properties and Applications. *RSC Adv.* **2021**, *11* (12), 6477−6503.

(7) Hippalgaonkar, K.; Wang, Y.; Ye, Y.; Qiu, D. Y.; Zhu, H.; Wang, Y.; Moore, J.; Louie, S. G.; Zhang, X. High Thermoelectric Power Factor in Two-Dimensional Crystals of MoS_2. *Phys. Rev. B* **2017**, *95* (11), 115407.

(8) Deng, T.; Gao, Z.; Qiu, P.; Zhou, Z.; Ming, C.; Liu, Z.; Li, Z.; Yang, S.; Wei, T.-R.; Wang, G.; et al. High Thermoelectric Power Factors in Plastic/Ductile Bulk $SnSe_2$-Based Crystals. *Adv. Mater.* **2023**, *36* (5), 2304219.

(9) Zhang, H.; Zhang, Z.; Zhan, Q.; Liu, D.; Zhao, P.; Cheng, Y. Recent Advances of Substitutionally Doped Tin Dichalcogenides. *J. Mater. Chem. C* **2022**, *10* (20), 7771−7782.

(10) Zhou, X.; Gan, L.; Tian, W.; Zhang, Q.; Jin, S.; Li, H.; Bando, Y.; Golberg, D.; Zhai, T. Ultrathin $SnSe_2$ Flakes Grown by Chemical Vapor Deposition for High-Performance Photodetectors. *Adv. Mater.* **2015**, *27* (48), 8035−8041.
(11) Xu, P.; Fu, T.; Xin, J.; Liu, Y.; Ying, P.; Zhao, X.; Pan, H.; Zhu, T. Anisotropic Thermoelectric Properties of Layered Compound $SnSe_2$. *Sci. Bull.* **2017**, *62* (24), 1663−1668.
(12) Zhou, C.; Yu, Y.; Zhang, X.; Cheng, Y.; Xu, J.; Lee, Y. K.; Yoo, B.; Cojocaru-Mirédin, O.; Liu, G.; Cho, S.-P.; et al. Cu Intercalation and Br Doping to Thermoelectric $SnSe_2$ Lead to Ultrahigh Electron Mobility and Temperature-Independent Power Factor. *Adv. Funct. Mater.* **2020**, *30* (6), 1908405.
(13) Kim, S. I.; Hwang, S.; Kim, S. Y.; Lee, W.-J.; Jung, D. W.; Moon, K.-S.; Park, H. J.; Cho, Y.-J.; Cho, Y.-H.; Kim, J.-H.; et al. Metallic Conduction Induced by Direct Anion Site Doping in Layered $SnSe_2$. *Sci. Rep.* **2016**, *6* (1), 19733.
(14) Wu, X.; Han, J.; Feng, Y.; Li, G.; Wang, C.; Ding, G.; Gao, G. Half-Metals and Half-Semiconductors in a Transition Metal Doped $SnSe_2$ Monolayer: A First-Principles Study. *RSC Adv.* **2017**, *7* (70), 44499−44504.
(15) Guo, X.; Shi, Y.; Ding, Y.; He, Y.; Du, B.; Liang, C.; Tan, Y.; Liu, P.; Miao, X.; He, Y.; et al. Indium-Doping-Induced Selenium Vacancy Engineering of Layered Tin Diselenide for Improving Room-Temperature Sulfur Dioxide Gas Sensing. *J. Mater. Chem. A* **2022**, *10* (42), 22629−22637.
(16) Chen, P.; Shang, J.; Yang, Y.; Wang, R.; Cheng, X. Annealing Tunes Interlayer Coupling and Optoelectronic Property of Bilayer $SnSe_2/MoSe_2$ Heterostructures. *Appl. Surf. Sci.* **2017**, *419*, 460−464.
(17) Wei, Y.; Li, J.; Zhang, D.; Zhang, B.; Zhou, Z.; Han, G.; Wang, G.; Prestipino, C.; Lemoine, P.; Guilmeau, E.; et al. Phase-Dependent Microstructure Modification Leads to High Thermoelectric Performance in *n*-Type Layered $SnSe_2$. *Acta Mater.* **2024**, *263*, 119504.
(18) Li, Z.; Shu, W.; Li, Q.; Xu, W.; Zhang, Z.; Li, J.; Wang, Y.; Liu, Y.; Yang, J.; Chen, K.; et al. Nondegenerate P-Type In-Doped SnS_2 Monolayer Transistor. *Adv. Electron. Mater.* **2021**, *7* (7), 2001168.
(19) Sheldrick, G. M. Crystal Structure Refinement with *SHELXL*. *Acta Crystallogr., Sect. C: Struct. Chem.* **2015**, *71* (1), 3−8.
(20) Sheldrick, G. M. SHELXT − Integrated Space-Group and Crystal-Structure Determination. *Acta Cryst. A* **2015**, *71* (1), 3−8.
(21) Schulze, H. G.; Foist, R. B.; Okuda, K.; Ivanov, A.; Turner, R. F. B. A Small-Window Moving Average-Based Fully Automated Baseline Estimation Method for Raman Spectra. *Appl. Spectrosc.* **2012**, *66* (7), 757−764.
(22) Acharya, S.; Srivastava, O. N. Occurrence of Polytypism in $SnSe_2$. *J. Cryst. Growth* **1981**, *55* (2), 395−397.
(23) Pałosz, B.; Gierlotka, S.; Lévy, F. Polytypism of $SnSe_2$ Crystals Grown by Chemical Transport: Structures of Six Large-Period Polytypes of SnSe2. *Acta Cryst. C* **1985**, *41* (10), 1404−1406.
(24) Tauc, J.; Grigorovici, R.; Vancu, A. Optical Properties and Electronic Structure of Amorphous Germanium. *Phys. Status Solidi B* **1966**, *15* (2), 627−637.
(25) Tauc, J. Optical Properties and Electronic Structure of Amorphous Ge and Si. *Mater. Res. Bull.* **1968**, *3* (1), 37−46.
(26) Garg, A. B.; Vie, D.; Rodriguez-Hernandez, P.; Muñoz, A.; Segura, A.; Errandonea, D. Accurate Determination of the Bandgap Energy of the Rare-Earth Niobate Series. *J. Phys. Chem. Lett.* **2023**, *14* (7), 1762−1768.
(27) Evans, B. L.; Hazelwood, R. A. Optical and Electrical Properties of $SnSe_2$. *J. Phys. D: Appl. Phys.* **1969**, *2* (11), 1507.
(28) Gonzalez, J. M.; Oleynik, I. I. Layer-Dependent Properties of SnS_2 and $SnSe_2$ Two-Dimensional Materials. *Phys. Rev. B* **2016**, *94* (12), 125443.
(29) Wood, D. L.; Tauc, J. Weak Absorption Tails in Amorphous Semiconductors. *Phys. Rev. B* **1972**, *5* (8), 3144−3151.
(30) Smith, A. J.; Meek, P. E.; Liang, W. Y. Raman Scattering Studies of SnS_2 and $SnSe_2$. *J. Phys. C: Solid State Phys.* **1977**, *10* (8), 1321.
(31) Weszka, J.; Daniel, P.; Burian, A.; Burian, A. M.; Nguyen, A. T. Raman Scattering in In_2Se_3 and InSe2 Amorphous Films. *J. Non-Cryst. Solids* **2000**, *265* (1), 98−104.
(32) Liu, C.; Huang, Z.; Wang, D.; Wang, X.; Miao, L.; Wang, X.; Wu, S.; Toyama, N.; Asaka, T.; Chen, J.; et al. Dynamic Ag^+-Intercalation with $AgSnSe_2$ Nano-Precipitates in Cl-Doped Polycrystalline $SnSe_2$ toward Ultra-High Thermoelectric Performance. *J. Mater. Chem. A* **2019**, *7* (16), 9761−9772.
(33) Rajbanshi, A.; Duong, D.; Thareja, E.; Shelton, W. A.; Jin, R. Thermoelectric Properties of SnSe and $SnSe_2$ Single Crystals. *Phys. Rev. Mater.* **2024**, *8* (2), 023601.
(34) Onose, Y.; Takeshita, N.; Terakura, C.; Takagi, H.; Tokura, Y. Doping Dependence of Transport Properties in $Fe_{1-x}Co_xSi$. *Phys. Rev. B* **2005**, *72* (22), 224431.
(35) Kajikawa, Y. Multi-Band Analysis of Temperature-Dependent Transport Coefficients (Conductivity, Hall, Seebeck, and Nernst) of Ni-Doped $CoSb_3$. *J. Appl. Phys.* **2016**, *119* (5), 055702.
(36) Plackowski, T.; Matusiak, M. Normal-State Ettingshausen, Seebeck, and Hall Effects in $La_{2-x}Sr_xCuO_4$. *Phys. Rev. B* **1999**, *60* (21), 14872−14882.
(37) Gorodynskyy, V.; Zdansky, K.; Pekárek, L.; Vacková, S. Temperature Change of Hall and Seebeck Coefficient Sign in InP Doped with Transition Metals. *Semicond. Sci. Technol.* **2004**, *19* (2), 203.
(38) Kayanuma, K.; Hiramatsu, H.; Hirano, M.; Kawamura, R.; Yanagi, H.; Kamiya, T.; Hosono, H. Apparent Bipolarity and Seebeck Sign Inversion in a Layered Semiconductor: LaZnOP. *Phys. Rev. B* **2007**, *76* (19), 195325.
(39) Jones, R. E.; Yu, K. M.; Li, S. X.; Walukiewicz, W.; Ager, J. W.; Haller, E. E.; Lu, H.; Schaff, W. J. Evidence for p-Type Doping of InN. *Phys. Rev. Lett.* **2006**, *96* (12), 125505.

https://doi.org/10.1021/acs.jpcc.4c02926
J. Phys. Chem. C 2024, 128, 11054−11062